

## Concept for a critical-angle transmission grating spectrometer for the AXIS probe

Hans M. Günther<sup>1</sup>,<sup>a,\*</sup> David A. Principe,<sup>a</sup> Ralf K. Heilmann<sup>1</sup>,<sup>a,b</sup> Peter Cheimets<sup>1</sup>,<sup>c</sup>  
Edward Hertz<sup>1</sup>,<sup>c</sup> and Randall Smith<sup>c</sup>

<sup>a</sup>MIT Kavli Institute for Astrophysics and Space Research, Massachusetts Institute of Technology, Cambridge, Massachusetts, United States

<sup>b</sup>Massachusetts Institute of Technology, Space Nanotechnology Laboratory, Cambridge, Massachusetts, United States

<sup>c</sup>Center for Astrophysics | Harvard & Smithsonian, Cambridge, Massachusetts, United States

**ABSTRACT.** The Advanced X-ray Imaging Satellite (AXIS) is a probe-class mission concept with a large collecting area with a point-spread-function of order 1 to 2 arcsec. We describe a possible X-ray grating spectrometer (XGS) that could be added to AXIS with minimal design changes to the telescope itself and costs a small fraction of the total mission budget. The XGS would be based on critical-angle transmission (CAT) gratings, a technology already matured for Arcus and Lynx. Using detailed ray-tracing, we investigate several options for subaperturing that provide a trade-off between effective area and spectral resolving power. Depending on how much of the full aperture is covered with gratings (e.g., 17% to 100%), we find a high spectral resolving power up to  $\lambda/\Delta\lambda = 4000$  can be achieved with effective area of 1500 cm<sup>2</sup> in the 1.2 to 2.8 nm range or  $\lambda/\Delta\lambda = 6000$  with effective area 500 cm<sup>2</sup>. An important benefit of CAT gratings is that they are mostly transparent at high energies, and thus hard x-rays can still be used for simultaneous imaging spectroscopy. We study different grating sizes and other enhancements, but even in the basic configuration an XGS can be added to AXIS to provide high-resolution spectral capabilities, opening a range of new science investigations. Our ray-tracing shows that this concept is mature and can be added to AXIS with minimal impact on other instruments. We discuss one exemplary science case that would be enabled by the XGS.

© 2023 Society of Photo-Optical Instrumentation Engineers (SPIE) [DOI: 10.1117/1.JATIS.9.2.024007]

**Keywords:** ray-tracing; x-ray optics; critical-angle transmission grating; AXIS; Rowland torus; grating spectroscopy

Paper 22114G received Nov. 21, 2022; revised May 5, 2023; accepted May 5, 2023; published May 22, 2023.

### 1 Introduction

Probe-class missions are located between NASA's medium explorer (MIDEX) programs and multi-billion dollar flagship missions. The Advanced X-ray Imaging Satellite (AXIS)<sup>1</sup> is a probe-class mission concept that would use an Si meta-shell approach to nest many precisely formed Si mirrors to achieve a high effective area about two orders of magnitude better than the Chandra X-ray observatory<sup>2</sup> while maintaining a point-spread-function (PSF) of 1 to 2 arcsec over a field of view radius of  $\approx 10$  arcmin instead of just the central 2 to 4 arcmin. Mirrors and detectors are optimized for similar energies as Chandra and XMM-Newton,<sup>3</sup> from about 0.3 to 10 keV.

\*Address all correspondence to Hans M. Günther, [hgünther@mit.edu](mailto:hgünther@mit.edu)

With these characteristics, AXIS will deliver much sharper images than the planned Athena mission.<sup>4,5</sup> AXIS mission science would target a few specific science cases, such as galaxy evolution and feedback, the growth of black holes, and active galactic nuclei in the high-redshift universe, but would importantly function as a proposal-driven observatory that provides unique capabilities to a large range of science questions.

AXIS imaging requires just the mirror and an imaging spectrometer such as a CCD array at the focal plane. The CCD (or similar device) will provide low-resolution spectroscopic capabilities, but particularly in the soft-x-ray band the best CCD energy resolution is only 70 eV. In this work, we show that a grating spectrometer can outperform a CCD in soft x-rays by more than two orders of magnitude in terms of resolving power and thus enable fundamentally new science investigations that resolve emission or absorption line profiles from stars, black holes, and galaxies, or detect weak absorption lines from, e.g., the warm-hot intergalactic medium superimposed on background continuum sources. While microcalorimeters achieve an energy resolution of a few eV, in the soft x-ray band that only corresponds to a resolving power of  $\approx 100$  and microcalorimeters require extensive cooling and engineering at high cost, which puts them out of reach for AXIS.<sup>6,7</sup>

The initial AXIS design does not include a grating spectrometer, but we show here that one can be added in future design iterations. We present a design based on critical-angle transmission (CAT) gratings, which can be mounted behind the mirror, either permanently or on a mechanism that folds in and out as with the Chandra high and low energy transmission gratings (HETG<sup>8</sup> and LETG<sup>9</sup>), which have been operated successfully for over 24 years. CAT gratings are blazed and diffract most light to just one side, where additional CCDs would be located to observe the diffracted photons.

CAT gratings<sup>10,11</sup> are one of the enabling technologies for the Arcus X-ray grating spectrometer (XGS) Explorer mission,<sup>12</sup> which was proposed as a MIDEX mission, but not selected by NASA. The MIDEX version of Arcus was designed for  $R > 3500$  with  $A_{\text{eff}}$  up to  $350 \text{ cm}^2$  in the band between 1.2 and 5.0 nm. CAT gratings were also selected for the design reference mission for an XGS on Lynx,<sup>13</sup> one of the four mission concepts studied in detail before the 2020 Decadal survey.<sup>14</sup>

We have performed extensive ray-trace studies for both Arcus<sup>15,16</sup> and Lynx/XGS.<sup>13</sup> In particular, the Lynx/XGS is quite similar to the proposed XGS for AXIS that we describe here and we refer the reader to Ref. 13 for aspects of the design and alignment tolerances not fully covered in this article. We first present an example for the type of science investigation that can be addressed with AXIS/XGS and not with any other existing or approved instrument; in the later sections, we describe the layout of AXIS/XGS and model its performance through ray-tracing.

## 2 Science Example

AXIS/XGS will deliver a spectral resolving power 5 to 10 times higher than any x-ray instrument ever flown and simultaneously provide more than one order of magnitude improvement in effective area compared with the gratings on Chandra and XMM-Newton. Because the PSF is four to five times narrower than XMM-Newton's PSF, AXIS/XGS can disentangle spectra from moderately crowded fields and obtain many grating spectra at once, when looking at, e.g., a stellar cluster; because of the effective area gain of several orders of magnitude compared with Chandra/HETGS, it can deliver a much better signal than Chandra. With this advancement, we can expect ground-breaking results in different fields of astrophysics. Here, we want to just present one example.

Most stars form from molecular clouds in gravitationally bound clusters. In the early stages of star formation before about 10 Myrs of age, protostars increase their mass by accumulating (accreting) gas and dust from their surrounding molecular cloud. Over time, gravitational contraction causes a star to spin up resulting in the formation of a circumstellar disk<sup>17</sup> and a powerful magnetic dynamo.<sup>18</sup> Stellar magnetic fields generated by these dynamos play an essential role in young stellar evolution as they facilitate the transfer of angular momentum between the star-disk system.<sup>19</sup> Moreover, x-rays generated by magnetically heated coronal plasma can affect circumstellar disk chemical evolution<sup>20</sup> and the photoevaporative dispersal of the disk,<sup>21</sup> constraining

the available time for planet formation. Recent models show the disk-wind mass loss rate is dominated by irradiation from soft x-rays between 0.1 and 1.0 keV.<sup>22</sup>

As a result of their rapid rotation and magnetic dynamos, young pre-main sequence stars are relatively bright x-ray sources with  $\sim 100$  times the  $L_X/L_{\text{bol}}$  of their more-evolved spectral counterparts on the main sequence. While thousands of nearby young stars have been imaged with x-ray observatories, such as Chandra, XMM-Newton, and ROSAT, much of the physical information provided by these soft (0.3 to 2 keV) emission-line dominated sources is indistinguishable when observed with the poor spectral resolution of CCD imaging provided by these observatories. Both Chandra and XMM-Newton have grating instruments to disperse photons achieving resolving powers of  $\sim 1000$ . Stellar spectra at these high resolutions provide important temperature and plasma density diagnostics capable of unambiguously characterizing the complex multi-temperature components that make up stellar coronae.<sup>23</sup> In particular, the temperature- and density-sensitive lines of H-like and He-like ions can be used to distinguish between the hot, low-density, dynamo-generated coronal emission components and “cool”  $\sim 3\text{MK}$  high density accretion shock plasma from material funneled along magnetic field lines from the disk onto the star.<sup>24</sup> While these instruments have provided a tantalizing view of the underlying physics governing about a dozen young star-disk systems, the poor effective area and extended PSF size off-axis of these telescopes limit our ability to observe pre-main sequence stellar physics at the age of planet formation to only the nearest and brightest young stars.<sup>24–27</sup>

There are two primary features of AXIS that, if leveraged with the inclusion of CAT gratings, can extend our current set of quality high resolution x-ray spectra of young stars from a few dozen to more than several hundred. This instrument design would be ideal for obtaining dozens of high-resolution x-ray spectra of young pre-MS stars in a single observation of a young stellar cluster (see Fig. 1). These observations could be performed for all nearby stellar clusters easily providing hundreds of high quality x-ray spectra over a much larger mass and age range than the dozen young stars currently in the achieves. Building large samples of x-ray spectra for stars

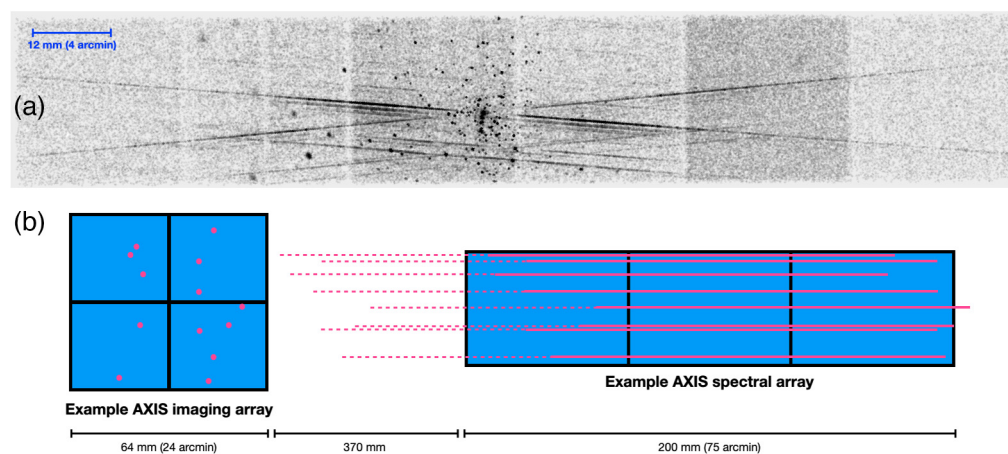


**Fig. 1** (a) Chandra High Energy Transmission Gratings (HETGS) observation (ObsID 8895) of the Orion Nebula Cluster star-forming region energy filtered between 0.5 and 8.0 keV. Data for this image were retrieved from the Chandra archive and processed with CIAO.<sup>28</sup> The gray scale in the image is scaled logarithmically and has been smoothed to emphasize the dispersed grating events. In the HETGS layout, the spectrum from each source is dispersed in an X shape on the detector. Several overlapping dispersed spectra can be seen. This 25 ks observation demonstrates the power of an instrument capable of achieving high spatial and spectral resolution for a dense region of point sources. Due to Chandra’s poor effective area compared to that proposed for AXIS, only the brightest few sources near the aim-point in the image produce enough counts for detailed high resolution spectral fitting. (b) Conceptual AXIS imaging and spectral array configuration to be used with CAT gratings. The exact number and dimensions of the detectors on the focal plane depends on the devices chosen, but approximate distances and dimensions are given (not to scale in the sketch). Light from the stars on the imaging array is dispersed and a spectral array is placed where grating efficiencies are highest (solid lines); there is a gap between the direct imaging detector and the spectral array where the signal is weak (dashed lines) and thus no detectors are needed. Dispersed spectra from several bright sources can be observed at the same time.

within a particular stellar cluster would finally allow us to compare plasma characteristics as a function of stellar age, mass, natal molecular cloud abundance, and metallicity.

Moreover, the proposed high effective area of AXIS would unlock a brand new science case for studying planet-formation. Planet-forming circumstellar disks absorb soft x-rays imprinting in the high resolution stellar X-ray spectrum a signature that can be used to unambiguously determine the abundance of line-of-sight circumstellar disk oxygen. The high spectral resolution oxygen absorption edge feature at  $\sim 550$  eV has been previously observed in the ISM using very bright background x-ray sources.<sup>29</sup> However, the high effective area of AXIS makes this science feasible for nearby pre-MS stars whose x-rays are viewed through their highly inclined circumstellar disks. Modeling of this feature in the ISM constrains oxygen abundance, the ratio of gas and solid state oxygen, and even dust grain mineralogy.<sup>30,31</sup> Bringing this technique to nearby circumstellar disks for the first time would provide a novel way to study gas composition and dust mineralogy for hundreds of disks at an era where it is becoming clear that oxygen plays a significant role in the chemical evolution of disks and the formation of planets.<sup>32–34</sup>

### 3 Spectrometer Design

The heart of a spectrometer is a collection of diffraction gratings. These will be positioned in the converging beam downstream of the mirrors. Since the resolving power  $R$  increases with the distance of the dispersed signal from the focal point of the mirror, it is beneficial to mount them in a structure closely behind the end of the mirrors.

#### 3.1 Assumptions on the Mirror

The mirror for AXIS is planned to be made from a number of Si meta-shells that are made from many independently manufactured plates.<sup>35</sup> Those plates are mounted in a stack that covers some range in angle and radius and is surrounded by a support structure to hold individual plates in place. The details and dimensions of these support structures will be refined as the AXIS concept matures. In our simulations, we thus do not track all details, but instead approximate the area covered by the mirror as a series of just a few concentric rings that represent the planned radius of the meta-shell modules. All finer structures (individual plates, the angular distribution of the support structures) are treated in a statistical way. They block just a certain fraction of the light without tracking their exact location.

We perform a ray-trace using our code for the simplified mirrors (iridium coated), optical and UV blocking filters, and imaging detectors. We determine the effective area that this simulation gives as  $11,500 \text{ cm}^2$ . The AXIS white paper<sup>1</sup> claims an effective area of  $7000 \text{ cm}^2$ , so we determine a scale factor between those two numbers of 0.61; one minus this number can be thought of as the fraction of the geometric area that is not actively concentrating light, e.g., because it hits the 0.5 mm thick “side” of a Si shell or because it hits some part of the mirror support structure. In that sense, all other simulations are scaled to a zero-order effective area of  $7000 \text{ cm}^2$  at 1 keV. If that area goes up or down, the effective area for the dispersed spectra scales the same way.

The mirror is simplified as a perfect lens in a single plane. This simplification would give a PSF with infinitesimal width. We thus add scatter in the plane of reflection and perpendicular to the plane of reflection (out of plane). If the PSF is dominated by figure errors of the mirror surface, the in-plane scatter would be much larger than the out-of-plane scatter. If, instead, it is dominated by alignment errors of Si-plates in a meta-shell module or between modules, both contributions might be similar. In most of our simulations, we assume that both contribute, with in-plane scatter just twice as large as out-of-plane scatter. A single, narrow piece of Si-mirror would give an elliptical PSF, but note that combining the PSFs of all meta-shell modules still gives a round PSF in the focal plane. However, we also run one scenario where in-plane and out-of-plane scatter are the same and thus the PSF of a single, narrow piece of the mirror would already be round (we call this scenario “round PSF” referring to the PSF per meta-shell module). To be conservative, we set up the simulations such that the total observed PSF combined from all meta-shell modules has a half-power diameter of 1 arcsec, a factor of two worse than in the AXIS white paper.<sup>1</sup> We do not consider diffraction from the aperture size of the individual mirror shells, because we estimate it to be small compared with the total mirror PSF.<sup>36,37</sup>

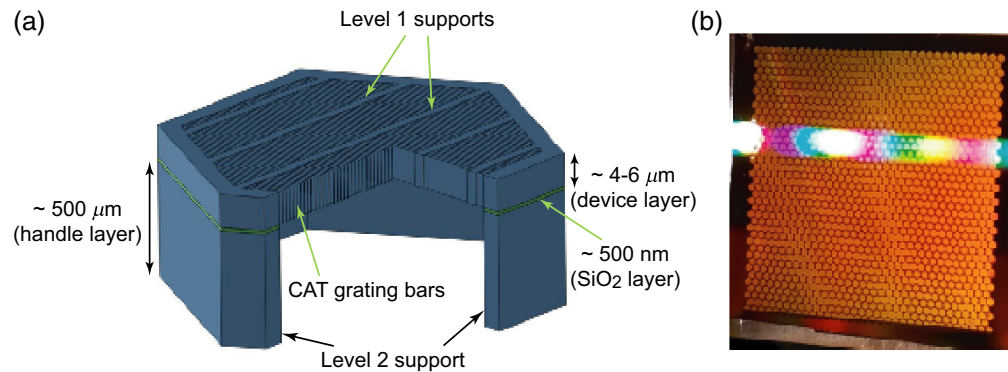


**Fig. 2** (a) Schematic depiction of the structural hierarchy of the CAT grating membrane (see text). (b) Photograph of a back-illuminated  $32 \times 32 \text{ mm}^2$  prototype CAT grating membrane, showing the hexagonal L2 mesh and optical diffraction from the L1 mesh.

### 3.2 CAT Gratings

CAT gratings have been under development for almost two decades.<sup>38–45</sup> Using processes compatible with mass-manufacturing, they are patterned Si-on-insulator (SOI) wafers and etched<sup>10,11</sup> to produce freestanding ultra-high aspect-ratio grating bars. CAT gratings are most efficient under a certain blaze angle, when photons do not pass parallel to the grating bars but instead “bounce off” the grating bar sides. The best angle depends on the energy range, the grating material, and the depth of the gratings.

Grating bars are held in place by a hierarchical series of support structures (see Fig. 2). The first is the L1 support on top of 2 mm wide hexagons (L2 support structure) etched out of the SOI handle layer. We assume that L1 and L2 structures cover about 10% of the geometric area each and reduce the photon throughput accordingly. This grating frame is then surrounded by a 1 mm wide solid Si frame, which can be bonded to a holder and mounted on a frame to hold the gratings in place. The ray-trace includes diffraction by the L1 and L2.<sup>46</sup>

The gratings we consider in this study are identical to those simulated for Lynx/XGS.<sup>13</sup> They have the same geometrical structure as the gratings produced as baseline proto-types for the MIDEX Arcus mission but are about 50% deeper ( $5.7 \mu\text{m}$  instead of  $4.0 \mu\text{m}$ ); the thickness of the L1 support structures is reduced from 9 to  $7 \mu\text{m}$ , and the thickness for the L2 support structures from 99 to  $70 \mu\text{m}$  to increase the grating efficiency. We keep the grating period of 200 nm but increase the gap between grating bars from the currently manufactured 140 to 160 nm. We consider pure Si gratings and, as a design option, gratings where the side walls are coated with a  $\sim 6 \text{ nm}$  thick layer of platinum.<sup>47</sup> Grating bars are supported by integrated Si bars running perpendicular to them (L1 support structure,  $5 \mu\text{m}$  period) and etched from the same layer. For high energies, the Si bars become highly transparent to x-ray photons and the structure acts as a phase-shifting grating dispersing photons into low orders (mostly 0,  $\pm 1$ ,  $\pm 2$ ).

Current gratings are made with a size up to  $32 \times 32 \text{ mm}^2$  for the Arcus Explorer mission<sup>12</sup> (see Fig. 2). These gratings can achieve  $>30\%$  absolute diffraction efficiency at 2.38 nm wavelength (sum over allblazed orders), including absorption by L1 and L2 supports.<sup>48</sup> Alignment is done with a laser reflection tool that can be used for both roll and yaw alignment.<sup>49</sup> Roll alignment of up to four CAT gratings performed in air was verified in x-rays to within 5 arcmin<sup>48,50</sup> well within the requirements.<sup>13</sup> Multiple gratings have been aligned to each other in a flight-like configuration and two simultaneously illuminated grating facets show a resolving power  $R_G = (1.3 \times 10^4)_{-0.5}^{+inf}(3\sigma)$ .<sup>51</sup> This shows that the resolving power of the full instrument we study here is not limited by manufacturing or alignment tolerances of the gratings. The pattern of the grating membranes and support structures is defined using  $4\times$  optical projection lithography on 200 mm wafers and pattern changes are straightforward to implement. Previous environmental testing showed that current gratings survive launch loads without affecting performance.<sup>50</sup> Thus, limited work is needed to evolve the current design of the gratings to the dimensions we are simulating here.

The XGS is designed with a Rowland torus geometry,<sup>52</sup> where gratings are located on the Rowland torus, defined by the radius of the tube  $r$  and the distance  $R$  from the center of the torus

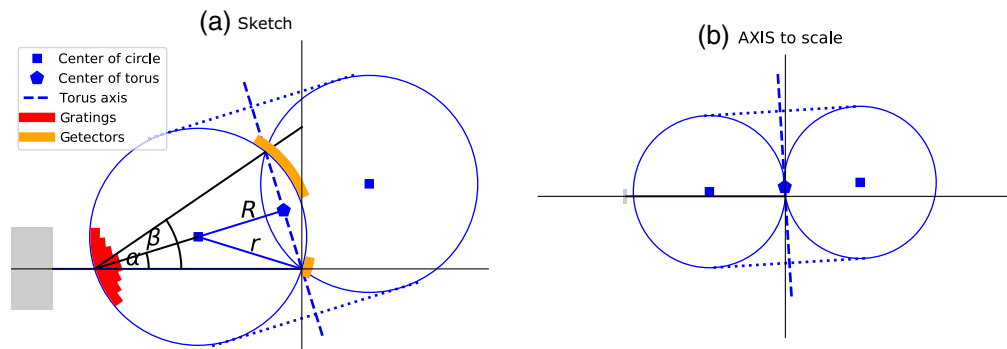


**Fig. 3** Layout of the AXIS/XGS. (a) Conceptual sketch; (b) To-scale. In both panels, the gray box on the left side indicates the mirror location; its focal point is at the intersection of the horizontal and vertical black lines. The drawing shows a cut through a plane, which contains the symmetry axis of the torus; two blue circles of radius  $r$  show the intersection of this plane with the torus and blue dotted lines help to visualize the torus position. For the parameters chosen, the two circles overlap.  $\alpha$  is chosen to be 2.2 times the blaze angle to make the blazed grating facets almost tangential to the Rowland Torus. In the sketch, the location of the detectors (orange) and the gratings (red) is indicated; they are not visible in the to-scale drawing because individual elements are too small. The gratings are located on the torus surface, not just in the cut-plane of this sketch.

to the center of the tube, see Fig. 3. The torus is tilted by an angle  $\beta$  with respect to the optical axis.<sup>15,53</sup> We chose  $\alpha$  to be 2.2 times the blaze angle and  $\beta = 2\alpha$ . That way, gratings with the chosen blaze angle of 1.6 deg are still mostly tangential to the surface of the torus, minimizing the average distance between any point on the flat gratings and the surface of the torus. The torus dimensions are optimized to position the gratings close to the end of the mirror to increase the distance between the focal point and the dispersed signal, as this increases the spectral resolving power.

### 3.3 Filters

Since x-ray detectors are also sensitive to optical and UV light, we add an optical blocking filter of 30 nm Al topped with 10 nm of aluminum oxide, which may be directly deposited on the detectors. Above that, we simulate a 45 nm layer of Kapton mounted on a 95% transmissivity metal mesh, which acts as contamination filter to prevent contamination build-up on cold detector surfaces.

### 3.4 Position of Detector

The geometry of CAT gratings favors diffraction orders that direct photons to a specific location (the “blaze peak”) located 400 to 600 mm (Fig. 4) from the focal point, where the detectors for the dispersed spectrum must be placed. The width of this peak depends on wavelength, the depth of the gratings, and the distribution of blaze angle (Sec. 4.1) for each grating. To keep the cost and requirements on additional cooling, power, and data volume down, we simulate just four CCD-ID94 devices. Those CCDs are rectangular with 2048 times 1024 pixels of 24  $\mu\text{m}$  size and together cover almost the entire blaze peak. In practice, one might want to use the same detector type that is also mounted in the imaging instrument in the focal plane to simplify integration and testing and later software development and calibration. Detector requirements for the dispersed signal are not very stringent. Since the signal is spread out, count rates are generally lower than in an imaging instrument, thus read-out can be slower and 24  $\mu\text{m}$  pixels simulated here already oversample the line-spread function and there is no benefit of higher spatial resolution.

Detectors for the dispersed signal are mounted following the Rowland-torus geometry. The imaging detector at the focal point of AXIS, which is planned anyway, can provide information on the zero-order image position for wavelength calibration without placing any additional requirements on that detector.

### 3.5 Ray-Trace Code

We use the Python-based, open source, Monte-Carlo code MARXS for our ray-trace.<sup>54,55</sup> The simulations for this work are run with a development version of MARXS to include

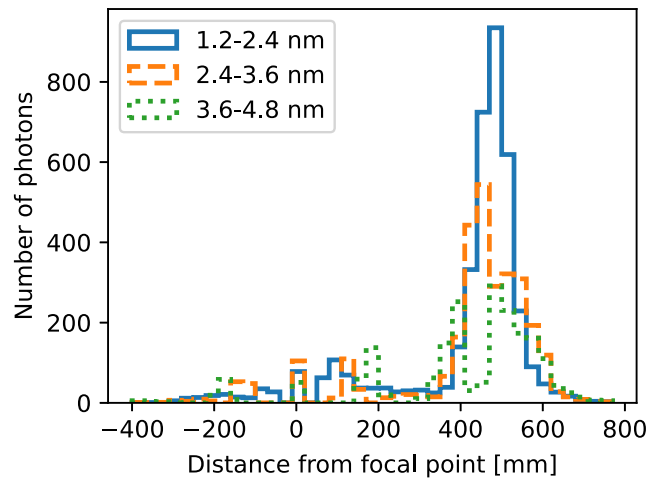


**Fig. 4** Ray-trace of a continuum source through AXIS/XGS. CAT gratings disperse photons of different energy into different orders, such that most of them end up in a narrow range of angles. The photon distribution has a clear peak at twice the blaze angle, which we call the blaze peak. Detectors only need to cover this narrow region at 400 to 600 mm distance from the focal point of the mirror to catch the vast majority of photons.

AXIS-specific code; that version is publicly accessible in the MARXS repository with commit hash: 3550974d0. Optical properties of materials such as diffraction or transmission probabilities are input from data tables and not calculated by MARXS itself.

## 4 Results

We study different configurations for AXIS and compare the effective area and resolving power. Some scenarios use gratings similar to what has been demonstrated for Arcus already, whereas others explore modifications that have not yet been demonstrated to the same level.

- The baseline scenario studied here uses  $30 \times 60 \text{ mm}^2$  flat gratings, where all gratings have exactly the same grating constant. They are arranged such that the short dimension is parallel to the dispersion direction and the long dimension to the cross-dispersion direction. About 1000 gratings are needed to cover the full aperture. In the following discussion and figures, simulations use this scenario unless otherwise noted. We choose this scenario as the “baseline” because flat, homogeneous gratings any larger reduce performance because rays hitting off center are either too far from the Rowland torus or too far from the nominal blaze angle.
- Using larger gratings means that fewer gratings are needed to cover the same geometric area, which reduces cost and also losses due to geometric coverage by the grating support structure. A 200 mm Si wafer can yield four  $60 \times 60 \text{ mm}^2$  gratings, thus these can be manufactured at a similar cost as  $30 \times 60 \text{ mm}^2$  gratings, but only half as many gratings have to be calibrated, mounted, and aligned.
- When gratings are flat, they deviate from the Rowland torus. This can be compensated by varying the grating period over the grating (chirp). Chirped gratings allow us to use very large gratings ( $60 \times 180 \text{ mm}^2$ ) without loss of resolving power. Chirped gratings have not yet been demonstrated. In principle, the chirp needed is different for every grating, but in practice, just two or three types of gratings will suffice,<sup>56</sup> keeping complexity and cost down and the total number of gratings is only about 150 to cover the entire aperture.
- Alternatively, the gratings can be bent in at least one dimension to follow the Rowland-torus more closely. Laboratory tests of (smaller) bent gratings indicate that the bending does not impact their throughput.<sup>57</sup> Bending is only worth the effort if large gratings are used, here  $60 \times 60 \text{ mm}^2$ .
- Finally, we present simulations where the PSF is dominated by alignment error (the “round PSF” scenario described in Sec. 3.1). A round PSF is the worst-case for a grating

spectrometer, because there is no benefit of subaperturing (using only a fraction of mirror aperture, chosen such that the resulting PSF is asymmetric and the dispersion direction is selected to make the spectral features narrow in dispersion direction), but we adjust the in-plane and out-of-plane scatter to keep the total mirror PSF at 1 arcsec HPD. Gratings are arranged as in the baseline scenario.

#### 4.1 Detailed Look at the Diffraction of 0.6 keV Photons

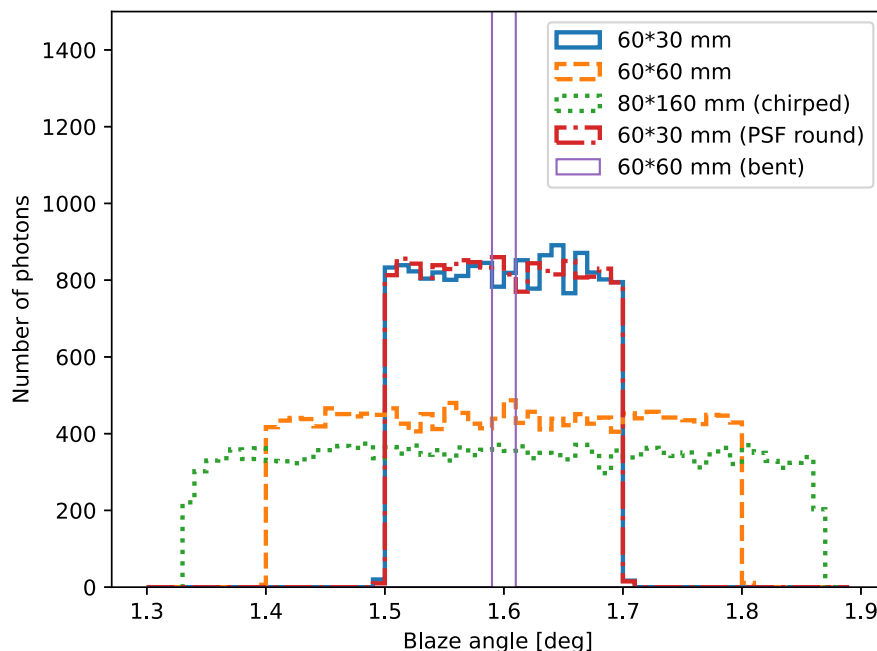
First, we simulated events at one specific energy close to the crucial O VII triplet at 2.1 nm and see how the diffracted orders look on the detector and what we can learn about subaperturing.

Figure 5 shows the distribution of blaze angles for the different scenarios. The position of the detectors is optimized for a specific blaze angle. For flat gratings of finite size, the blaze angle is set for the central ray. That means that photons of a converging beam that pass the grating in a different location will have a different value for the blaze angle. The larger the grating, the larger the range of blaze angles. This leads to broader blaze peak (Fig. 4) and photons will be lost unless the read-out detector is expanded. Bending the gratings with a radius of 8.5 m (the average distance of a grating from the focal point) reduces the spread of blaze angles to ensure that all photons intersect the grating at the blaze angle that gives the best diffraction efficiency.

#### 4.2 Line Spread Function and Subaperturing

We define the resolving power as:  $R = \frac{\lambda}{\Delta\lambda} = \frac{d_x}{\text{FWHM}}$  where  $\lambda$  is the wavelength of a spectral line with negligible intrinsic width, and  $\Delta\lambda$  is the observed width (the line spread function (LSF)) of this feature. The FWHM is the full width at half maximum of the event distribution, measured in the dispersion direction, and  $d_x$  is the distance between the center of a diffracted order and the center of the zeroth order.

Figure 6 shows the distribution of 0.6 keV photons diffracted into the sixth order on the detector for our scenarios. Figure 6(a) shows the position of the gratings in the mirror aperture plane. Gratings are colored according to the azimuthal angle from the dispersion direction. The Rowland torus is symmetric to reflection on the dispersion axis ( $y = 0$  line in the figure) and this is represented in the color of the gratings in the panel. In the other panels, photons are colored according to the grating they passed through. Photons going through gratings with different azimuthal angles have different spatial distributions on the detector. Photons that went through



**Fig. 5** Distribution of blaze angles over all gratings for different grating sizes. For the bent gratings, all photons fall into the same bin, which is cut off in the figure for display purposes.

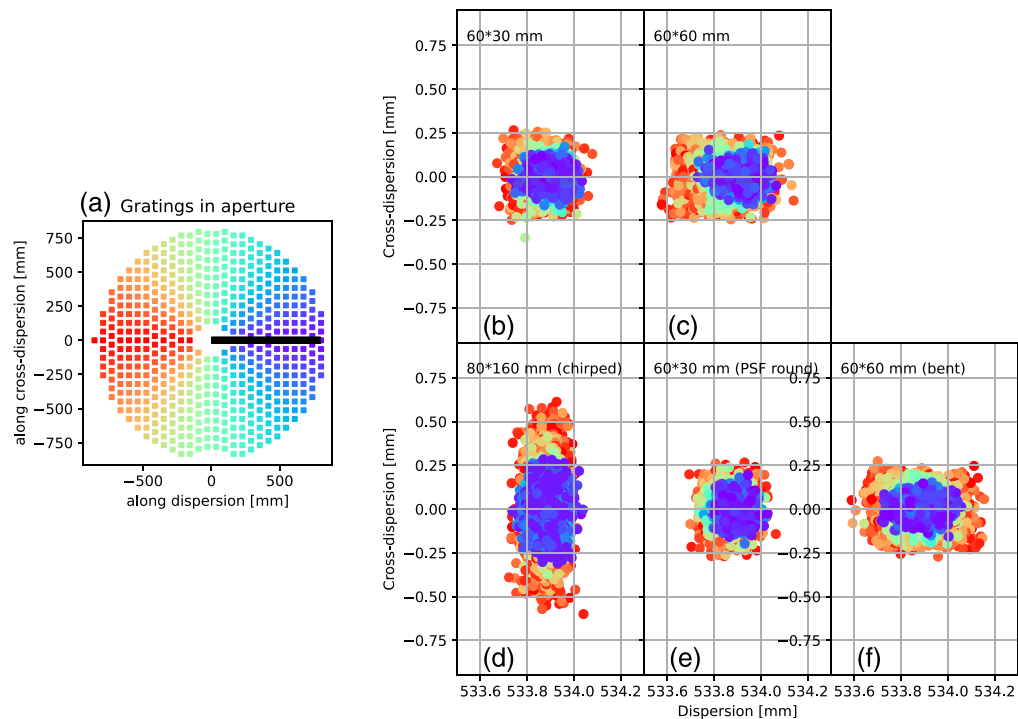


**Fig. 6** (a) Position of gratings in the aperture plane. The gratings are color coded by angle relative to the dispersion direction (black arrow). (b)–(f) Distribution of photons with exactly 0.6 keV in the sixth order for different CAT grating sizes and mirror scattering properties. Each dot represents a single detected photon, color coded by the grating it passed. Note that the x and y axes are on different scales.

the gratings displayed in purple are distributed narrower than the red points; using only the former photons will deliver a lower FWHM and thus higher  $R$ .

When the spectrum is extracted for analysis, the distribution in cross-dispersion direction (y axis in Fig. 6) does not matter for the width of the spectral feature. Figure 7 shows the photon distributions in Fig. 6 collapsed on the dispersion axis. To understand how subaperturing (filling only part of the aperture with gratings) can influence  $R$ , the figure displays the photon distribution resulting from gratings in narrow sectors, e.g., a pie-shaped sector containing just photons that pass through gratings with an absolute azimuthal angle of 30 to 60 deg [light blue line in Fig. 7, corresponding to the light blue gratings in Fig. 6(a)].

For all the scenarios, the photons passing through gratings located perpendicular to the dispersion direction (light green line) have the sharpest peaks. The other lines differ from the green line in two ways. They are often wider and in some cases their peaks are shifted. The width of the distribution is due to the intrinsic mirror PSF and the fact that the gratings deviate from the Rowland torus. In our simulations, the gratings are placed such that the center of each grating matches the Rowland torus. Because of the tilt of the torus, gratings located in the range 60 deg to 90 deg are almost tangential to the torus surface and have the smallest average deviation and thus the sharpest LSF. Larger gratings have larger average deviations than smaller gratings and thus the green LSF in the 60 mm  $\times$  30 mm scenarios is narrower than in the 60 mm  $\times$  60 mm scenario. Gratings located at larger or smaller angles cannot be tangential because they have to be rotated to match the blaze angle specification and deviate more from the surface of the torus, leading to wider LSFs (lower  $R$ ). Thus, these simulations show that a higher  $R$  can be achieved if only certain parts of the aperture are filled with gratings. As the size of the grating increases, the spots get wider and  $R$  is reduced, unless gratings are chirped or bent.

A second effect is the shift in the peak of the LSF between the green line and the other angles' ranges; this is due to the fact that for gratings tangential to the Rowland torus, the average distance of the grating to the detector is larger than for gratings that intersect the Rowland torus. The latter is required in some locations to keep the blaze angle in the specified range.

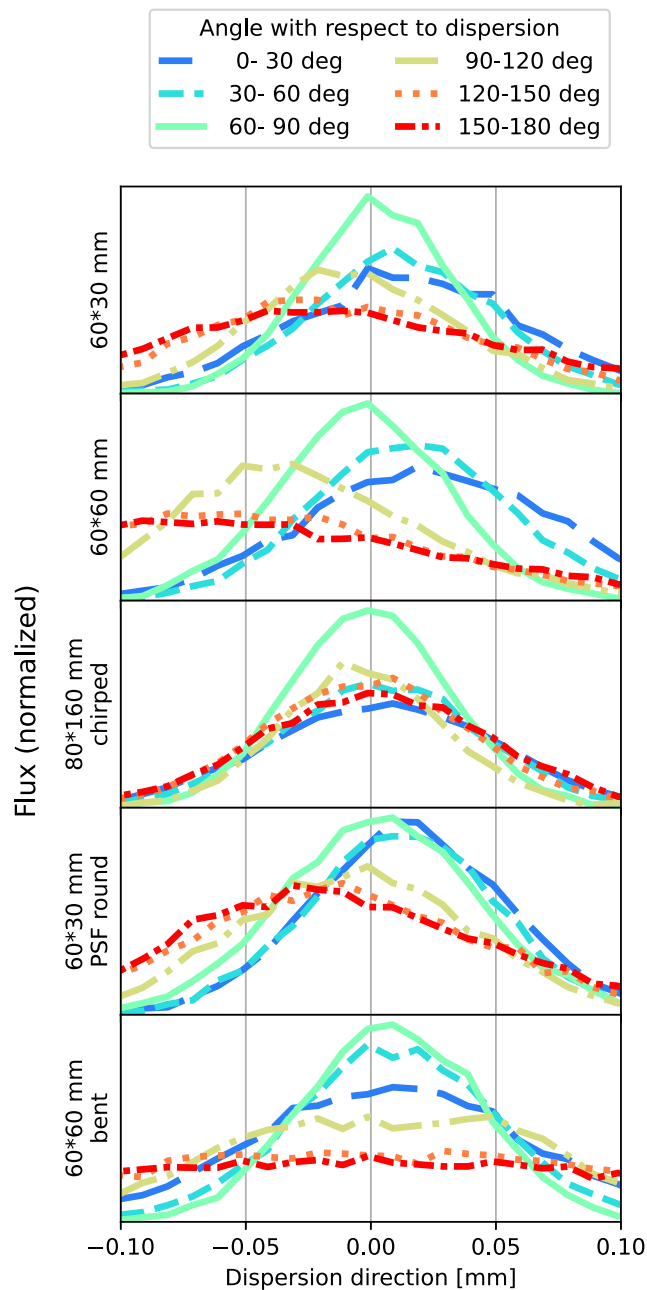


**Fig. 7** Distribution of detected photons in the dispersion direction for different subaperture angles. The flux is shown with a different, arbitrary normalization for each panel. The zero point of the x-axis is set to be the center of the simulated distribution. This is the same data as in Fig. 6, but displayed as a histogram along the cross-dispersion direction; the colors of the lines in this figure match the colors of the gratings in Fig. 6(a).

The two scenarios  $60 \text{ mm} \times 30 \text{ mm}$  and  $60 \text{ mm} \times 30 \text{ mm}$  (scatter) use the same gratings but differ in the scatter properties of the mirror. If the mirror PSF is dominated by figure errors and scattering, then subaperturing will increase  $R$  a lot more than in the scenario where the PSF is dominated by off-center errors (PSF round).

Figure 8 shows the trade-off between effective area and  $R$  for different fractions of the aperture filled with gratings and different scenarios. Of the five scenarios studied, large, chirped gratings provide the best performance but also require the most development in grating manufacturing. Without chirping, smaller gratings provide better  $R$ , but a lower effective area than larger gratings. Comparing the two scenarios  $60 \text{ mm} \times 60 \text{ mm}$  (orange) and  $60 \text{ mm} \times 60 \text{ mm}$  (bent, purple), we can see that the bent gratings achieve a better effective area for a given

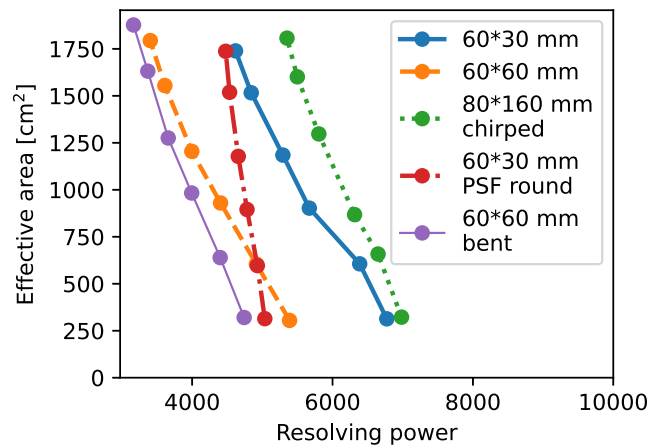


**Fig. 8** Each colored line in this plot is one scenario (grating size, chirp yes/no, etc.). The line connects simulations with different subaperturing angle and specific angles are marked with dots (top to bottom filling 100%, 83%, 67%, 50%, 33%, and 17% of the total space with gratings). This figure corresponds to an energy of 0.6 keV.

filling factor, because all photons interact with the grating at the same blaze angle, but  $R$  suffers because the bent gratings deviate more from the Rowland torus than flat gratings. For all scenarios, we can choose to populate only part of the aperture with gratings, reducing the effective area and increasing  $R$ . That choice has to be made based on the science requirements for high-resolution grating spectroscopy.

#### 4.3 Resolving Power and Effective Area

To evaluate the resolving power and effective area for a range of photon energies, we run ray-traces for the canonical case of  $30 \times 60$  mm gratings with no bending or chirping. In this early phase of the design, we limit ourselves to a coarse wavelength grid and thus to not resolve all details like chip gaps.

Figure 9 shows the effective area and resolving power  $R$ . The latter is essentially constant with wavelength, because photons are all diffracted into the blaze peak. Thus, for a given spectrograph and mirror,  $R$  just depends on the distance between the focal point and the diffracted order. The effective area of the diffracted signal increases above about 1.2 nm where the Si grating bar side walls reflect the photons efficiently. The dip around 2 nm is due to one of the two or three relevant orders hitting a chip gap. However, since we see more than one diffraction order for most wavelengths, some signal is still available. Chip gaps can further be mitigated through dithering or placing the source in a specific location to avoid spectral regions of interest to fall on chip gaps. There should be more chip gaps, but the wavelength resolution of the simulations here is so low that most of them are just stepped over.

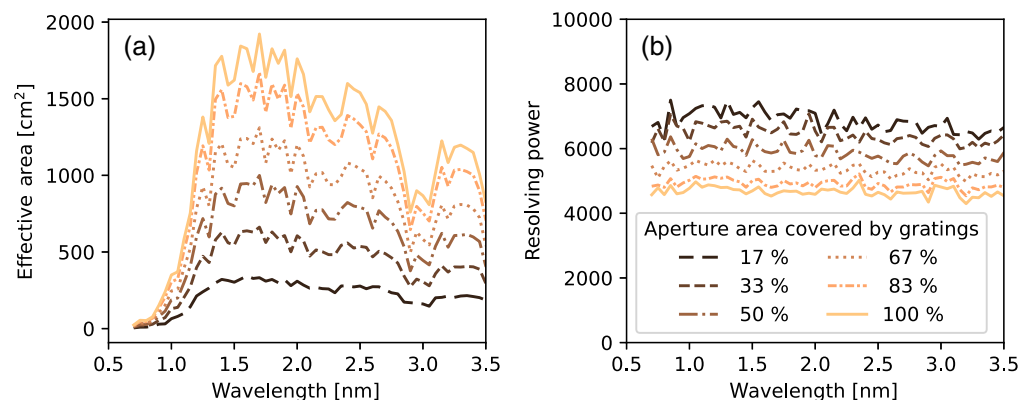


**Fig. 9** (a) Effective area and (b) resolving power for different subaperturing angles in the baseline scenario.

## 5 Cost and Technical Readiness Level

The XGS requires two new systems to be added to AXIS: gratings and detectors. The requirements on the detectors are relatively simple and detectors can be chosen from a variety of CCDs with high flight heritage or could be chosen to match the detectors used for direct imaging. In that way, there is an additional cost to procure the detectors but no impact on the technology maturation plan for AXIS, only minimal software development for grating data reduction, and no added technical risk.

CAT gratings have been matured for the Lynx and Arcus/MIDEX mission concepts and have been tested in an x-ray beam in a flight-like configuration including alignment of several grating elements in a grating holder, individual gratings have been tested environmentally for temperature and vibration.<sup>58</sup> As such, we assess the technology at TRL 6 for individual flat gratings with dimensions about 30 mm on each side and the L1 and L2 parameters used in that test. An XGS with these TRL 6 gratings would lower the effective area up to 50% compared with our baseline scenario because the thicker L1 and L2 structures and additional grating holders for the smaller gratings block more light. The resolving power would be unchanged. Little development is needed to reach TRL 6 for our baseline scenario; essentially, one needs to write a different mask for the UV lithography and repeat environmental testing. The scenarios with bending and chirping require more development and testing.

Since the marginal cost of manufacturing additional gratings is small and the same number of detectors will be needed in any case, the cost does not change much if only part of the aperture is covered with gratings.

The power requirements of the grating petal are minimal since it only requires power to be moved into and out of the optical path between observations and possibly coarse temperature control. The power requirements of the detectors depend on the detector technology chosen and the number of detectors. From an operational point of view, planning and scheduling XGS observations of single point sources works the same as for direct imaging observations. For observations of crowded fields, particular roll angles of the spacecraft might be required, which places constraints on the scheduling of observations.

## 6 Discussion

We have shown through ray-tracing that AXIS/XGS can reach  $R > 6000$  with an effective area around 500 cm<sup>2</sup> in the conservative case of covering just 33% of the aperture with CAT gratings in the baseline scenario. AXIS can reach an effective area around 1500 cm<sup>2</sup> at  $R = 4000$ , if the entire aperture is covered. With this design, AXIS/XGS will outperform all existing or accepted future x-ray high-resolution spectroscopy missions by a wide margin. The CAT gratings simulated here are straightforward modifications of gratings that have already been manufactured and been aligned and tested in an x-ray beamline;<sup>51</sup> the total efficiency of the simulated gratings is about a factor of two better than the gratings that were planned for the Arcus MIDEX mission. The improvement is a sum of several small steps (larger grating facets to reduce dead area from mounting structures, deeper gratings, wider distances between support structures, thinner grating bars, and support structures), some of which are well underway now, e.g., deeper gratings have already been tested in an x-ray beamline and been shown to reach the  $R$  values required.<sup>51</sup> Still, in the unlikely case that none of the improvements succeed, the predicted effective area could be up to a factor two lower than the numbers given above.

Considering energies of 0.5 keV as an example, the AXIS/XGS with 33% coverage of the aperture will have about 40 times the effective area and at least 10 times the resolving power of Chandra/LETGS; it will have two orders of magnitude more effective area than Chandra/HETGS at launch and almost four orders of magnitude more than Chandra/HETGS has today and a factor of 5 better resolving power;<sup>8</sup> and compared with XMM/RGS our ray-traces show more than one order of magnitude increase in  $R$  and about one order of magnitude in an effective area. Microcalorimeters such as those on XRISM<sup>59</sup> and Athena X-IFU do not reach above  $R = 200$  at low energies, a critical bandpass for diagnosing plasma temperature and density for soft x-ray sources such as young pre-main sequence stars. Such a dramatic jump in capability will lead to significant new discoveries in many areas in astrophysics.

Further refinements of the design shown here can be made, but the most important input is to set the science requirements on  $R$  and effective area to decide on the subaperturing angle. Options for the CAT gratings with lower TRL include a coating with a metal like Pt, which will increase the reflectivity at higher energies and increase the energy range where  $R = 5000$  is possible to 2 keV, and bending and chirping as simulated above. For the design of the spectrograph, we can optimize the tilt of the Rowland torus or split gratings such that dispersed gratings fall on different channels such as the HEG and MEG in Chandra/HETG.<sup>8</sup> A third of the aperture could be covered with gratings to reach  $R > 6000$  with an effective area around 500 cm<sup>2</sup> while the remaining area could be covered with gratings that diffract in slightly different direction, so another 1000 cm<sup>2</sup> effective area is simultaneously available at a  $R > 3000$ —still a factor of a few more than any existing instrument.

Another, more complex, option is to build three separate spectrographs, each covering 33% of the aperture and dispersing on its own strip of CCDs. In that case, more CCDs are needed, but  $R$  is not compromised, so each spectrograph would reach  $R > 6000$  with a combined effective area  $>1500$  cm<sup>2</sup> in the 1.2 to 2.8 nm range.

While not simulated in this work, CAT gratings allow relatively easy alignment tolerances that can be met by machining alone in many degrees of freedom. Reference 13 found that  $1\sigma$  tolerances are typically several mm for translations and arcminutes or even degrees for rotations. AXIS/XGS has a larger mirror PSF than used in that study, so  $R$  will be lower than it would have been for Lynx/XGS<sup>13</sup> anyway, and thus alignment requirements for AXIS/XGS would be even looser.

## 7 Summary

In this article, we present a concept for an XGS for the AXIS probe. Based on CAT grating technology that has been developed and matured over the last decade or so, the spectrometer can deliver a resolving power up to  $R = 6000$  and an effective area up to  $>1500$  cm<sup>2</sup> in the soft x-ray band (1.2 to 2.8 nm) for potentially several dozen sources in the field of view depending on their location in the sky and roll angle of the telescope. There is a trade-off between  $R$ , effective area and complexity. In the basic configuration, the spectrometer can reach  $R = 4000$  and an effective area of 1500 cm<sup>2</sup> or  $R = 6000$  and an effective area of 500 cm<sup>2</sup> (1.2 to 2.8 nm). It is important to note that CAT grating based spectrometers have fairly loose alignment requirements that can be met by machining alone in many degrees of freedom,<sup>13</sup> reducing time-consuming and costly alignment steps. Effective area and  $R$  for the AXIS/XGS are orders of magnitude better than existing instruments and will open entirely new science areas such as the detection of weak absorption lines in the warm-hot intergalactic medium, determining elemental abundances in proto-planetary disks through absorption edges, and kinematically resolving emission lines from accretion and winds in stars.

The XGS requires two new elements to be introduced to the AXIS design: CAT gratings just behind the mirror, and detectors for the dispersed light in the focal plane. The TRL for both components is high and the total cost of the XGS would be just a small fraction of the total budget. The gratings are mostly transparent at higher energies but could also be moved into and out of the beam as in the highly successful Chandra gratings, so there would be no impact at all on observations that do not specifically request dispersed spectra. Moreover, observations with the gratings inserted will simultaneously provide undispersed (zeroth order) images with the standard imaging detectors on AXIS. We present different design options based on different grating sizes and there is a trade-off where more development of larger bend or chirped gratings can improve performance and reduce cost, but we show that all designs studied provide unmatched scientific opportunities in the soft x-ray band.

---

## Acknowledgments

Support for this work was provided in part through NASA Grant NNX17AG43G and Smithsonian Astrophysical Observatory (SAO) Contract SV3-73016 to MIT for support of the *Chandra* X-Ray Center (CXC), which is operated by SAO for and on behalf of NASA under Contract NAS8-03060. The simulations make use of Astropy, a community-developed core Python package for astronomy,<sup>60,61</sup> numpy,<sup>62</sup> and IPython.<sup>63</sup> Displays are done with matplotlib.<sup>64</sup>

## References

1. R. Mushotzky et al., “The advanced x-ray imaging satellite,” *Bull. Am. Astron. Soc.* **51**, 107 (2019).
2. M. C. Weisskopf et al., “An overview of the performance and scientific results from the Chandra X-Ray observatory,” *Publ. Astron. Soc. Pac.* **114**, 1–24 (2002).
3. F. Jansen et al., “XMM-Newton observatory. I. The spacecraft and operations,” *Astron. Astrophys.* **365**, L1–L6 (2001).
4. M. J. Collon et al., “Making the ATHENA optics using silicon pore optics,” *Proc. SPIE* **9144**, 91442G (2014).
5. M. J. Collon et al., “Silicon pore optics development for ATHENA,” *Proc. SPIE* **9603**, 96030K (2015).
6. N. Meidinger et al., “Wide field imager instrument for the advanced telescope for high energy astrophysics,” *J. Astron. Telesc. Instrum. Syst.* **1**, 014006 (2015).
7. M. S. Tashiro, “XRISM: x-ray imaging and spectroscopy mission,” *Int. J. Mod. Phys. D* **31**, 2230001 (2022).
8. C. R. Canizares et al., “The Chandra high-energy transmission grating: design, fabrication, ground calibration, and 5 years in flight,” *Publ. Astron. Soc. Pac.* **117**, 1144–1171 (2005).
9. A. C. Brinkman, “Description and performance of the low energy transmission grating spectrometer on-board Chandra,” in *APS April Meeting Abstr., APS Meeting Abstr.*, p. J8.005 (2000).
10. R. K. Heilmann et al., “Diffraction efficiency of 200-nm-period critical-angle transmission gratings in the soft x-ray and extreme ultraviolet wavelength bands,” *Appl. Opt.* **50**, 1364 (2011).
11. R. K. Heilmann, A. R. Brucoleri, and M. L. Schattenburg, “High-efficiency blazed transmission gratings for high-resolution soft x-ray spectroscopy,” *Proc. SPIE* **9603**, 960314 (2015).
12. R. K. Smith et al., “Arcus: exploring the formation and evolution of clusters, galaxies, and stars,” *Proc. SPIE* **10397**, 103970Q (2017).
13. H. M. Günther and R. K. Heilmann, “Lynx soft x-ray critical-angle transmission grating spectrometer,” *J. Astron. Telesc. Instrum. Syst.* **5**, 021003 (2019).
14. J. A. Gaskin et al., “Lynx X-Ray observatory: an overview,” *J. Astron. Telesc. Instrum. Syst.* **5**, 021001 (2019).
15. H. M. Günther et al., “Performance of a double tilted-Rowland-spectrometer on Arcus,” *Proc. SPIE* **10397**, 103970P (2017).
16. H. M. Günther et al., “Ray-tracing Arcus in phase A,” *Proc. SPIE* **10699**, 106996F (2018).
17. H. Masunaga and S.-I. Inutsuka, “A radiation hydrodynamic model for protostellar collapse. II. The second collapse and the birth of a protostar,” *Astrophys. J.* **531**, 350–365 (2000).
18. R. W. Noyes et al., “Rotation, convection, and magnetic activity in lower main-sequence stars,” *Astrophys. J.* **279**, 763–777 (1984).
19. F. Gallet and J. Bouvier, “Improved angular momentum evolution model for solar-like stars,” *Astron. Astrophys.* **556**, A36 (2013).
20. V. Akimkin et al., “Protoplanetary disk structure with grain evolution: the ANDES model,” *Astrophys. J.* **766**, 8 (2013).
21. R. Alexander et al., “The dispersal of protoplanetary disks,” in *Protostars and Planets VI*, H. Beuther et al., Eds., p. 475, University of Arizona Press, Tucson (2014).
22. B. Ercolano et al., “The dispersal of protoplanetary discs - II: photoevaporation models with observationally derived irradiating spectra,” *MNRAS* **508**, 1675–1685 (2021).
23. D. P. Huenemoerder, C. R. Canizares, and N. S. Schulz, “X-ray spectroscopy of II Pegasi: coronal temperature structure, abundances, and variability,” *Astrophys. J.* **559**, 1135–1146 (2001).
24. J. H. Kastner et al., “Evidence for accretion: high-resolution x-ray spectroscopy of the classical T Tauri Star TW Hydrae,” *Astrophys. J.* **567**, 434–440 (2002).
25. H. M. Günther et al., “X-ray accretion signatures in the close CTTS binary V4046 Sagittarii,” *Astron. Astrophys.* **459**, L29–L32 (2006).
26. D. P. Huenemoerder et al., “Evidence for accretion in the high-resolution x-ray spectrum of the T Tauri Star system Hen 3-600,” *Astrophys. J.* **671**, 592–604 (2007).
27. A. Telleschi et al., “High-resolution x-ray spectroscopy of T Tauri stars in the Taurus-Auriga complex,” *Astron. Astrophys.* **468**, 443–462 (2007).
28. A. Fruscione et al., “CIAO: Chandra’s data analysis system,” *Proc. SPIE* **6270**, 62701V (2006).
29. E. Costantini et al., “XMM-Newton observation of 4U 1820-30. Broad band spectrum and the contribution of the cold interstellar medium,” *Astron. Astrophys.* **539**, A32 (2012).
30. J. Wilms, A. Allen, and R. McCray, “On the absorption of x-rays in the interstellar medium,” *Astrophys. J.* **542**, 914–924 (2000).
31. C. Pinto et al., “Interstellar medium composition through x-ray spectroscopy of low-mass x-ray binaries,” *Astron. Astrophys.* **551**, A25 (2013).
32. E. Gaidos, “What are little worlds made of? Stellar abundances and the building blocks of planets,” *Astrophys. J.* **804**, 40 (2015).

33. S. Krijt et al., “CO depletion in protoplanetary disks: a unified picture combining physical sequestration and chemical processing,” *Astrophys. J.* **899**, 134 (2020).
34. A. Banzatti et al., “Hints for icy pebble migration feeding an oxygen-rich chemistry in the inner planet-forming region of disks,” *Astrophys. J.* **903**, 124 (2020).
35. W. W. Zhang et al., “High-resolution, lightweight, and low-cost x-ray optics for the Lynx observatory,” *J. Astron. Telesc. Instrum. Syst.* **5**, 021012 (2019).
36. B. D. Chalifoux et al., “Simulations of film stress effects on mirror segments for the Lynx x-ray observatory concept,” *J. Astron. Telesc. Instrum. Syst.* **5**(2), 021004 (2019).
37. L. Raimondi and D. Spiga, “Mirrors for x-ray telescopes: Fresnel diffraction-based computation of point spread functions from metrology,” *Astron. Astrophys.* **573**, A22 (2015).
38. M. Ahn, R. K. Heilmann, and M. L. Schattenburg, “Fabrication of ultrahigh aspect ratio freestanding gratings on silicon-on-insulator wafers,” *J. Vac. Sci. Technol. B: Microelectron. Nanometer Struct.* **25**, 2593 (2007).
39. K. Flanagan et al., “Spectrometer concept and design for x-ray astronomy using a blazed transmission grating,” *Proc. SPIE* **6688**, 66880Y (2007).
40. M. Ahn, R. K. Heilmann, and M. L. Schattenburg, “Fabrication of 200 nm period blazed transmission gratings on silicon-on-insulator wafers,” *J. Vac. Sci. Technol. B: Microelectron. Nanometer Struct.* **26**, 2179 (2008).
41. P. Mukherjee et al., “Plasma etch fabrication of 60:1 aspect ratio silicon nanogratings with 200 nm pitch,” *J. Vac. Sci. Technol. B* **28**, C6P70–C6P75 (2010).
42. A. Bruccoleri et al., “Fabrication of nanoscale, high throughput, high aspect ratio freestanding gratings,” *J. Vac. Sci. Technol. B: Microelectron. Nanometer Struct.* **30**, 06FF03 (2012).
43. A. R. Bruccoleri et al., “Nanofabrication advances for high efficiency critical-angle transmission gratings,” *Proc. SPIE* **8861**, 886119 (2013).
44. A. Bruccoleri et al., “Potassium hydroxide polishing of nanoscale deep reactive-ion etched ultrahigh aspect ratio gratings,” *J. Vac. Sci. Technol. B* **31**, 06FF02 (2013).
45. A. R. Bruccoleri, R. K. Heilmann, and M. L. Schattenburg, “Fabrication process for 200nm-pitch polished freestanding ultrahigh aspect ratio gratings,” *J. Vac. Sci. Technol. B* **34**, 06KD02 (2016).
46. H. M. Günther and R. K. Heilmann, “Design progress on the Lynx soft x-ray critical-angle transmission grating spectrometer,” *Proc. SPIE* **11118**, 111181C (2019).
47. R. K. Heilmann et al., “Critical-angle x-ray transmission grating spectrometer with extended bandpass and resolving power > 10,000,” *Proc. SPIE* **9905**, 99051X (2016).
48. R. K. Heilmann et al., “Blazed transmission grating technology development for the Arcus x-ray spectrometer explorer,” *Proc. SPIE* **10699**, 106996D (2018).
49. J. Song et al., “Scanning laser reflection tool for alignment and period measurement of critical-angle transmission gratings,” *Proc. SPIE* **10399**, 1039915 (2017).
50. R. K. Heilmann et al., “Critical-angle transmission grating technology development for high resolving power soft x-ray spectrometers on Arcus and Lynx,” *Proc. SPIE* **10399**, 1039914 (2017).
51. R. K. Heilmann et al., “X-ray performance of critical-angle transmission grating prototypes for the Arcus mission,” *Astrophys. J.* **934**, 171 (2022).
52. K. P. Beuermann, H. Braeuninger, and J. Truemper, “Aberrations of a facet-type transmission grating for cosmic x-ray and XUV spectroscopy,” *Appl. Opt.* **17**, 2304–2309 (1978).
53. R. K. Heilmann et al., “Critical-angle transmission grating spectrometer for high-resolution soft x-ray spectroscopy on the International X-ray Observatory,” *Proc. SPIE* **7732**, 77321J (2010).
54. H. M. Günther, J. Frost, and A. Theriault-Shay, *Chandra-Marx/Marxs: VI.1*, Zenodo (2017).
55. H. M. Günther, J. Frost, and A. Theriault-Shay, “MARXS: a modular software to ray-trace x-ray instrumentation,” *Astron. J.* **154**, 243 (2017).
56. H. M. Günther and R. K. Heilmann, “Lynx grating spectrometer design: optimizing chirped transmission gratings,” *Proc. SPIE* **11444**, 1144488 (2020).
57. S. N. T. Heine et al., “Laboratory progress in soft x-ray polarimetry,” *Proc. SPIE* **10399**, 1039916 (2017).
58. R. K. Heilmann et al., “X-ray performance of critical-angle transmission grating prototypes for the Arcus mission,” *Astrophys. J.* **934**, 171 (2022).
59. M. Tashiro et al., “Status of x-ray imaging and spectroscopy mission (XRISM),” *Proc. SPIE* **11444**, 1144422 (2020).
60. Astropy Collaboration et al., “Astropy: a community Python package for astronomy,” *Astron. Astrophys.* **558**, A33 (2013).
61. Astropy Collaboration et al., “The astropy project: building an open-science project and status of the v2.0 core package,” *Astron. J.* **156**, 123 (2018).
62. S. van der Walt, S. C. Colbert, and G. Varoquaux, “The NumPy array: a structure for efficient numerical computation,” *Comput. Sci. Eng.* **13**, 22–30 (2011).

63. F. Perez and B. E. Granger, "IPython: a system for interactive scientific computing," *Comput. Sci. Eng.* **9**, 21–29 (2007).
64. J. D. Hunter, "Matplotlib: a 2D graphics environment," *Comput. Sci. Eng.* **9**, 90–95 (2007).

**Hans M. Günther** is a research scientist at MIT. He received his undergraduate degree in 2005 and his PhD in physics from the University of Hamburg, Germany, in 2005 and 2009, respectively. After that, he worked at the Harvard-Smithsonian Center for Astrophysics and came to MIT in 2015. He is currently the lead developer of MARX, the ray-tracing software used for the Chandra X-ray observatory. His science interests are in star formation using data from the radio to x-rays.

**David A. Principe** is a research scientist at MIT. He received his Bachelor of Science degree in astrophysics from Ohio University and his PhD from the Rochester Institute of Technology in 2009 and 2014, respectively. After a 2-year postdoctoral research fellowship at the Universidad Diego Portales in Santiago, Chile, he became a postdoctoral research associate at MIT. His current work as a research scientist involves supporting the Chandra X-ray Observatory and studying young stellar evolution.

**Ralf K. Heilmann** is a principal research scientist at the MIT Kavli Institute for Astrophysics and Space Research and the associate director of the Space Nanotechnology Laboratory (SNL). He received his Diploma in physics from the FAU Erlangen/Nürnberg in 1991, and his MS degree in 1993, and his PhD in 1996 in physics from Carnegie Mellon University. After a postdoc at Harvard, he joined the SNL and has since focused on advanced lithography and the development of x-ray optics for astronomy.

**Peter Cheimets** is a business development lead and head of SAO's smallSat program. He received his BS degree in mechanical engineering from MIT in 1974, his MS degree in dynamics and controls from Stanford in 1981, and his Master of Science degree in engineering management from Tuft University in 2007. He has developed EUV and x-ray missions for the Smithsonian Astrophysical Observatory for 25 years.

**Edward Hertz** is a project/mechanical engineer at SAO with over 30 years of experience in the design and development of complex instruments used for astronomical and astrophysical data collection. He has directed the efforts of multi-disciplined engineering and technical teams from project conception through optical alignment and subassembly integration. He received his BS degree in mechanical engineering with a minor in engineering management from Tufts University in 1983.

**Randall Smith** is the associate director of Science at the Center for Astrophysics | Harvard and Smithsonian and leader of a number of x-ray grating mission proposals. His science interests include understanding the formation and evolution of galaxies as well as the interstellar medium and the physics of hot plasma emission.